SCIENCE CHINA Materials ARTICLES

mater.scichina.com link.springer.com

Published online 7 April 2020 | https://doi.org/10.1007/s40843-020-1278-9
Sci China Mater 2020, 63(7): 1171–1181

Nb_2O_5 nanotubes on carbon cloth for high performance sodium-ion capacitors

Rui Jia[1,2], Yuan Jiang[3], Rui Li[1], Ruiqing Chai[2], Zheng Lou[2], Guozhen Shen[2*] and Di Chen[1*]

ABSTRACT **Hybrid sodium-ion capacitors (SICs) bridge the gap between the supercapacitors (SCs) and batteries and have huge potential applications in large-scale energy storage. However, designing appropriate anode materials with fast kinetics behavior as well as long cycle life to match with the cathode electrodes remains a crucial challenge. Herein, Nb_2O_5 nanotubes and nanowire-to-nanotube homo-junctions were directly grown on the carbon cloth (CC) *via* a simple hydrothermal process through regulating the pH value of solution. The as-prepared Nb_2O_5@CC nanotubes displayed a high reversible capacity of 175 mA h g^{-1} at the current density of 1 A g^{-1} with the coulombic efficiency of 97% after 1500 cycles. Besides, the SICs fabricated with Nb_2O_5@CC and activated carbon (AC) electrode materials showed a high energy density of 195 W h kg^{-1} at 120 W kg^{-1}, a power density of 7328 W kg^{-1} at 28 W h kg^{-1} and 80% of the capacitance retention after 5000 cycles. Additionally, the flexible SIC devices can operate normally at various bendable conditions. The Nb_2O_5@CC nanotubes in this work can be promising electrode materials in flexible and wearable energy storage devices.**

Keywords: nanotubes, homojunctions, Nb_2O_5, sodium-ion capacitors

INTRODUCTION

With the development of modern society, energy storage is becoming more and more important in portable electronics, electrical vehicles and intelligent transportation industries [1–6]. Till now, supercapacitors (SCs) and lithium-ion batteries (LIBs) are two kinds of primary energy storage units that have been comprehensively investigated. Although SCs can provide high power densities and long operating life, the low energy density limits their practical applications. As for LIBs, they are characterized by high energy densities as well as low power densities. In the past decade, lithium-ion capacitors (LICs) owning the combined advantages of both SCs and LIBs were rapidly developed. However, the high cost of lithium limits their application [7,8]. On the other hand, metallic sodium has similar chemical properties with lithium and possesses abundant reserves on the earth. Consequently, replacing the LICs with sodium-ion capacitors (SICs) as new energy storage devices is an important research topic [9–11].

The storage mechanism of the SICs is based on Faradic reactions of battery-type anode and adsorption/desorption of capacitor-type cathode. Generally, the cathode electrodes are carbon materials. The anodes are mainly focused on metal oxides (e.g., V_2O_5, TiO_2, Nb_2O_5 and MnO_2), nitrides (VN), chalcogenides (MoS_2, SnS_2 and $MoSe_2$), disordered carbon, MXenes and NASICON [12–23]. Recently, Nb_2O_5 has attracted much attention due to the large interlayer distance of 0.39 nm in (001) lattice plane, which is larger than the radius of Na^+ ions (1.02 Å) [14]. In addition, Nb_2O_5 possesses high chemical stability and has extensive applications in energy storage, liquid crystal display and electronic ceramics. Nevertheless, the conductivity of Nb_2O_5 is inferior, which needs to be enhanced to boost their electrochemical properties. For example, Lim *et al.* [16] fabricated SICs using Nb_2O_5@carbon core-shell structure combined with reduced graphene oxide (rGO) as anode and activated carbon (AC) (MSP-20) as cathode, giving a high energy density of 76 W h kg^{-1} and the maximum power density of 20,800 W kg^{-1}. Tong *et al.* [24] prepared SICs with anode materials of graphene sandwiched between two layers of mesoporous Nb_2O_5 nanosheets and AC as cathode, delivering the maximum energy/power densities of 56.1 W h kg^{-1} as well as 7200 W kg^{-1}. Besides, Wang *et al.* [14] synthesized Gr-Nb_2O_5 composites through growing

[1] School of Mathematics and Physics, University of Science and Technology Beijing, Beijing 100083, China
[2] State Key Laboratory for Superlattices and Microstructures, Institute of Semiconductors, Chinese Academy of Sciences, Beijing 100083, China
[3] Robert Frederick Smith School of Chemical and Biomolecular Engineering, Cornell University, Ithaca, NY 14853, USA
* Corresponding authors (emails: chendi@ustb.edu.cn (Chen D); gzshen@semi.ac.cn (Shen G))

graphene shells on the T-Nb_2O_5 nanowires, which was used as anode to construct the SICs with AC cathode. The Gr-Nb_2O_5//AC SICs obtained high energy and power densities of 112.9 W h kg^{-1} and 5330 W kg^{-1}, respectively. Much endeavor has been made to boost the conductivity and electrochemical properties of the Nb_2O_5 electrode materials, but there is still a large space of optimizing the structure design to improve the specific electrochemical performance of the SICs.

Herein, Nb_2O_5 with nanotubes and nanowire-on-nanotube homo-junctions on carbon cloth (CC) was grown *via* a simple hydrothermal method in the presence of pyridine. The as-fabricated SIC devices consisting of tubular Nb_2O_5@CC and AC as anode and cathode showed good electrochemical performances, including a high energy density of 195 W h kg^{-1} at the power density of 120 W kg^{-1} and the maximum power density of 7328 W kg^{-1} at the energy density of 28 W h kg^{-1}. Furthermore, the design of tubular Nb_2O_5@CC with short ion transport pathway benefits the cycling stability of the materials. The interconnected conductive CC can effectively enhance the electron transport. The flexible packaging of SICs also exhibited stable electrochemical properties under different bendable conditions.

EXPERIMENTAL SECTION

Synthesis

Nb_2O_5 was prepared through a simple hydrothermal method as shown in Fig. 1 Firstly, the CC substrate was treated with hydrochloric acid, followed by cleaning with acetone, ethanol and deionized (DI) water under ultrasonic processing, respectively. Then, 0.3 g of $C_4H_4NNbO_9 \cdot xH_2O$ was dissolved into a mixed solution of 12 mL ethanol and 18 mL *N*,*N*-dimethylformamide (DMF) at 80°C under constant stirring. After injection of 2 mL pyridine, HCl solution (1 mol L^{-1}) as pH regulator was dropped into the solution. The obtained solution and CC substrate were placed in the autoclave, which was heation of to 200°C for 24 h. After cooling down to room temperature, the products were gathered and rinsed with DI water and ethanol. In the following step, the materials were dried in the vacuum oven at 80°C for 12 h. Finally, the freshly prepared products underwent annealing treatment at 500°C in air for 3 h. During this procedure, several comparing experiments were carried out through changing pH values of the precursor solution ranging from 4.8–5.2, 4.5–4.7 to 4.0–4.4, and the relevant Nb_2O_5 products with nanotubes and nanowire-on-nanotube homo-junctions assigned as HJ-1 and HJ-2 were successfully obtained on the CC substrate, respectively. Furthermore, spherical Nb_2O_5 products were also prepared with the similar process without pyridine.

Characterizations

Small-angle X-ray scattering (SAXS) and wide-angle X-ray diffraction (XRD) tests were carried out with a Bruker D8 Advance X-Ray diffractometer with radiation from a Cu target (Kα, λ=0.15406 nm). Scanning electron microscope (SEM) of NanoSEM650-6700F was used to measure the surface morphologies of products. Transmission electron microscopy (TEM) measurements were

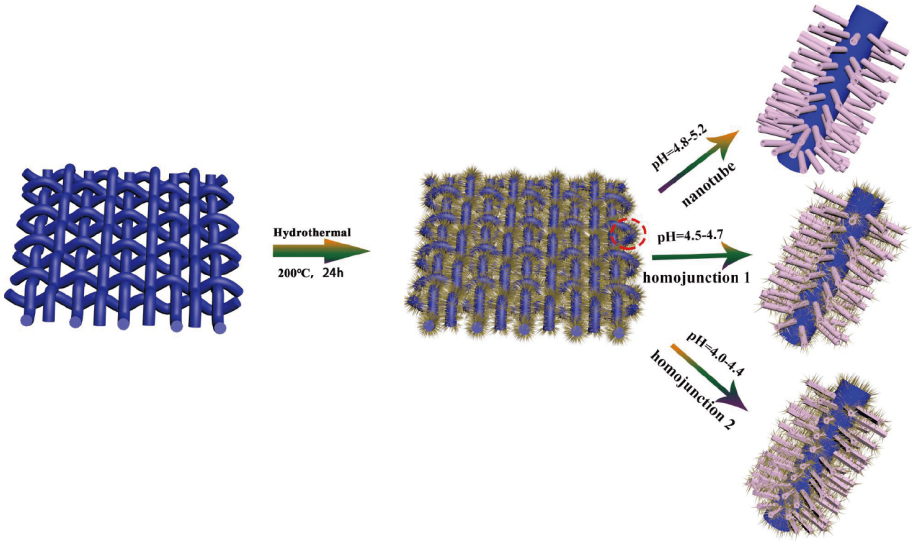

Figure 1 Schematic illustration of the growth of Nb_2O_5-based products on carbon cloth.

conducted with the equipment of JEOLJEM-2010HT. X-ray photoelectron spectroscopy (XPS) of Escalab 250-Xi was used to analyze the surface chemical constitution. The Brunauer-Emmett-Teller (BET) as well as pore distribution was investigated by ASAP 2460 instrument.

Electrochemical measurements

The electrochemical properties of the Nb_2O_5@CC materials were examined by assembling into CR2032 half-cells in the Ar-filled glove box using Na chip as the counter and reference electrodes with the potential of 0.01–3.0 V. The average amount of Nb_2O_5 materials on the CC was about 1 mg cm^{-2}. In the process of measurement, 1.5 mol L^{-1} $NaClO_4$ in the organic solvent of ethylene carbonate (EC):dimethyl carbonate (DMC) (1:1 in *v*:*v*) with 5% fluoroethylene carbonate (FEC) additive and glass fiber GF/D acted as electrolyte and separator. For comparison, Nb_2O_5 nanowire-on-nanotube homo-junctions and commercial Nb_2O_5 powders were also characterized in half-cells as electrode materials. To fabricate sodium ion batteries, the AC (BET > 2000 m^2 g^{-1}) was chosen as the electrode and prepared through mingling it with conductive carbon black and PVDF binder at the weight ratio of 8:1:1 in *N*-methyl pyrrolidone (NMP) solvent. Then the AC slurries was cast on the aluminum foils and dried in the vacuum oven at 80°C for 12 h. The electrochemical properties of AC were also tested in CR2032 half cells with Na chips in the voltage of 3.0–4.3 V. Furthermore, the SICs were prepared by using tubular Nb_2O_5@CC as anode, AC as cathode and the same separator and electrolyte in the half cells. Before assembling the SICs device, tubular Nb_2O_5@CC was pre-sodiated with Na chip at 0.1 A g^{-1} within the potential range of 0.01–3.0 V for three cycles and then discharged to 0.1 V. The pre-sodiated tubular Nb_2O_5@CC film was disassembled and then used as anode to fabricate SICs with AC as cathode in the mass ratio of 1:2. Flexible SIC full cells were also encapsulated with a thin Al-plastic film for practical applications. Galvanostatic charge-discharge (GCD) curves of the half cells were carried out with a multichannel battery testing system (Land-CT2001A). The CHI 760 electrochemical workstation was applied to test the electrochemical performance of the prepared SICs from 0 to 4.0 V and the cyclic voltammetry (CV) curves of the half cells. The current densities were on the basis of the total mass of the active materials in the SICs.

RESULTS AND DISCUSSION

The morphologies and microstructures of the as-obtained Nb_2O_5@CC materials at different pH levels were observed through SEM and TEM, respectively. Fig. 2a displays the SEM image of the Nb_2O_5 products obtained at the pH value of 4.8~5.2, which are uniformly grown on carbon fibers. Inset of Fig. 2a shows that the as-prepared Nb_2O_5

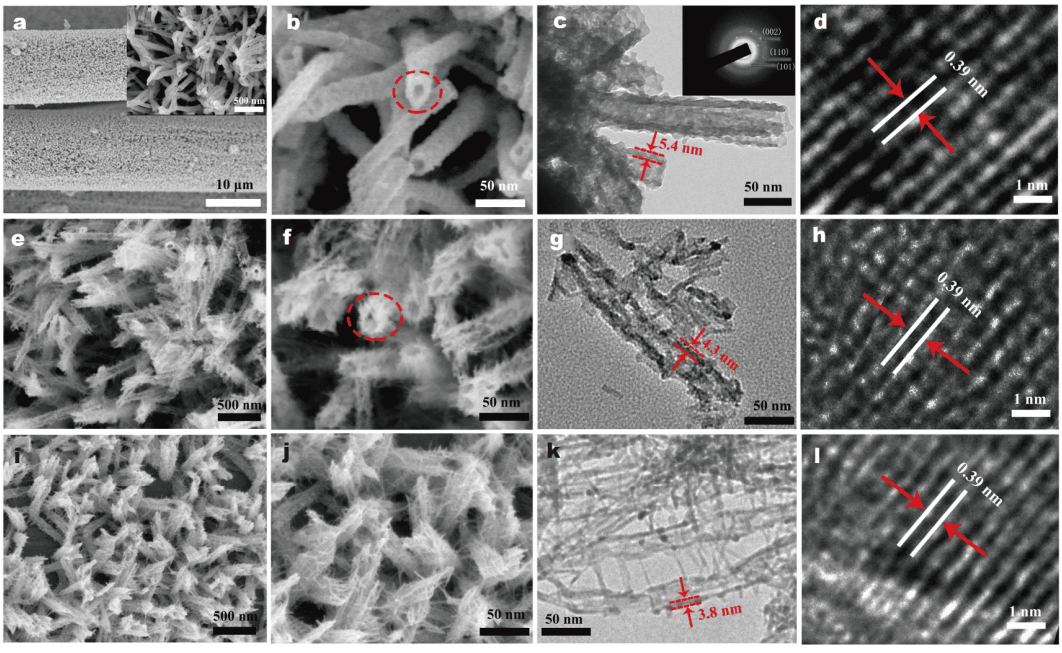

Figure 2 SEM, TEM and HRTEM images of the Nb_2O_5-based products at different pH values: (a–d) pH 4.8–5.2, (e–h) pH 4.5–4.7 and (i–l) pH 4.0–4.4.

products are of one-dimensional (1D) hollow structures. Fig. 2b displays the magnified SEM image, in which the red dotted circle further shows the typical tubular structure of the products with rough surface. Fig. 2c exhibits the corresponding TEM image of the Nb_2O_5 nanotubes with a uniform external diameter of about 30 nm as well as the wall thickness of around 5.4 nm, respectively. The selected area electron diffraction (SAED) pattern in Fig. 2c inset shows the polycrystalline nature. The high-resolution TEM (HRTEM) image in Fig. 2d manifests the legible lattice fringe of 0.39 nm in consistence with the (001) crystal face of Nb_2O_5, which is suitable for fast Na^+ diffusion. When the pH value of the solution dropped down to 4.5–4.7, the nanowire-on-nanotube homo-junctions (assigned as HJ-1) with similar external diameter of about 30 nm were prepared as shown in Fig. 2e, f. The red remark in Fig. 2f indicates that the central stems remain hollow structure. From the TEM images in Fig. 2g and Fig. S1, it can be obviously seen that many short nanowires and nanoplates with the length of 10–20 nm directly grow on the surface of the nanotubes with the thickness of tube wall of 4.3 nm, forming nanowire-on-nanotube homo-junctions. The HRTEM image in Fig. 2h presents the interplanar spacing of 0.39 nm, in accordance with the (001) crystal face of Nb_2O_5. Further decreasing the pH value to 4.0–4.4 resulted in similar homo-junctions (HJ-2) with longer nanowires as displayed in Fig. 2i, j. Moreover, Fig. 2k shows the TEM image of the homo-junctions with the wall thickness of 3.8 nm and the average length of the nanowires of 35 nm. Fig. 2l exhibits the HRTEM image of HJ-2, in which the interplanar distance of 0.39 nm could be indexed to the (001) lattice plane of Nb_2O_5.

With the pH value decreasing, the wall thickness of three tubular products got thinning with the external diameters almost unchanged. As for the two homo-junctions, the nanowires on the nanotube grew longer with the enhanced acidity. Interestingly, a large number of aggregated nanospheres with the average diameter of about 100 nm were directly obtained on the carbon fibers without pyridine under similar conditions as shown in Fig. S2. Thus, pyridine in this process can effectively guide Nb_2O_5 to form 1D construction, similar to other reports [25,26]. In addition, the acid solution in this system played important roles in the formation of Nb_2O_5 nanostructures, which not only controlled the crystalline phases and structures of the electrode materials, but also acted as the etching agent to grow the hollow microstructures [27–30]. Therefore, the fabrication of Nb_2O_5 nanotubes and homo-junctions with series of pH values in this work could be attributed to the synergetic effect between pyridine and the acid solution.

The surface chemical constitution of the Nb_2O_5 products was characterized by XPS. Fig. 3a displays the XPS spectrum survey of the Nb_2O_5 nanotubes with signals of C, Nb and O, confirming the formation of Nb_2O_5 sam-

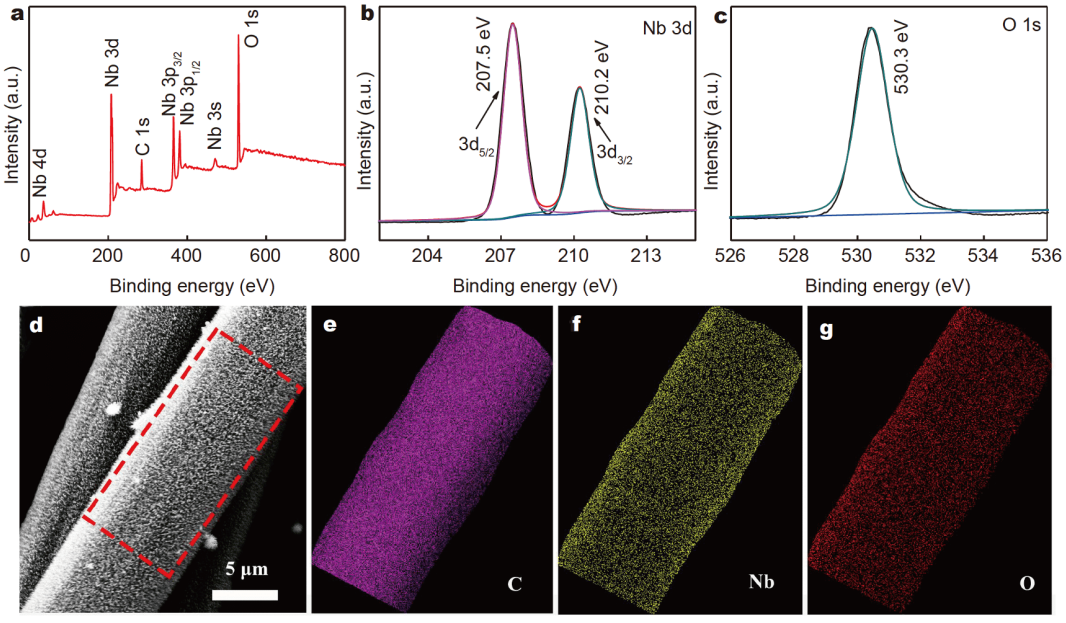

Figure 3 (a) XPS spectrum survey of the Nb_2O_5 nanotubes. (b, c) High resolution XPS spectra of Nb 3d and O 1s of Nb_2O_5 nanotubes. (d–g) SEM image and the corresponding element mappings of Nb_2O_5@CC nanotubes.

ples. Fig. 3b further shows the high resolution XPS spectrum of Nb 3d, where the two peaks at 207.5 and 210.2 eV represent Nb $3d_{5/2}$ and Nb $3d_{3/2}$, respectively. Fig. 3c exhibits the O 1s spectrum with the peak at 530.3 eV responding to the Nb–O bond [14]. The element distributions of Nb_2O_5@CC nanotubes were characterized by element mapping technique in Fig. 3d–g. It clearly shows that Nb and O evenly distribute in the products, which steadily anchor on the carbon fibers. Moreover, similar XPS results were also observed in other Nb_2O_5 products including nanowire-on-nanotube homo-junctions and spheres as presented in Fig. S3, illustrating the formation of pure Nb_2O_5 products with various microstructures on the CC substrate.

The crystal structures of various Nb_2O_5 products were characterized by XRD. Fig. 4a shows the XRD patterns of three products and all diffraction peaks can be indexed to Nb_2O_5 with orthorhombic phase (JCPDS 30-0873) [16]. SAXS study was also conducted in order to characterize the microstructures of the three samples. As shown in Fig. 4b, the distinct peak located at 0.42°, 0.39° and 0.38° are observed for nanotubes, HJ-1 and HJ-2, respectively, demonstrating the long-range order mesoporous structure of the three samples. Moreover, the diffraction peak shifts to lower angle, illustrating that the pore-to-pore distance becomes wide [31].

Besides, N_2 adsorption-desorption isotherms of the Nb-based products with various nanostructures suggest the process of gradual adsorption and desorption (type IV isotherms), as shown in Fig. S4, manifesting the features of mesoporous materials. All results are in accordance with the SAXS results. And the measured BET surface area of the Nb_2O_5 nanotubes is 260 m^2 g^{-1}, larger than that of HJ-1 (194 m^2 g^{-1}) and HJ-2 (172 m^2 g^{-1}), respectively. The pore size distribution curves in Fig. 4c display the average pore sizes of the nanotubes, HJ-1 and HJ-2 are 8.2, 10.9 and 11.8 nm, respectively, which are all larger than the radius of Na^+ ions. And the corresponding pore volumes change from 0.66, 0.58 to 0.48 cm^3 g^{-1}. As we know, larger pore volume means more effective contacting area between the electrode materials and electrolyte, which can facilitate chemical reactions. For example, the adsorption experiment of Nb_2O_5 nanotubes on CC (Nb_2O_5@CC) was operated by immersing the samples (containing 10 mg of Nb_2O_5) into 50 mL of methylene-blue (MB) solution (20 mg L^{-1}). After 2 h, 90.5% of MB was adsorbed, implying a high adsorption ratio of Nb_2O_5@CC nanotubes (Fig. S5). Inset in Fig. S5 shows that the color of MB turns pale after adsorption.

To probe the sodium storage performance of the Nb_2O_5@CC products with various nanostructures, we first assembled CR2032 coin cells by using the as-prepared Nb_2O_5-based samples as anode and Na chip as counter electrode with the electrolyte of 1.5 mol L^{-1} $NaClO_4$ in the organic solvent of EC:DMC (1:1 in *v*:*v*) with 5% FEC additive. Fig. 5a shows the CV curves of the Nb_2O_5@CC anodes with different nanostructures tested in the potential range from 0.01 to 3.0 V at the sweep rate of 1 mV s^{-1}. The similar shape of the CV curves indicates the same electrochemical reaction process. Additionally, according to the computational formula of capacitance based on CV curves:

$$C = A / (v \times m \times \Delta E), \quad (1)$$

where C is the capacitance, A is the integral area, v is the scan rate, m is the mass of active materials and ΔE is the voltage range. The capacitance of Nb_2O_5@CC nanotubes (400 F g^{-1} or 0.4 F cm^{-2}) calculated from the CV curve is relatively higher than that of HJ-1 (343 F g^{-1} or 0.34 F cm^{-2}), HJ-2 (273 F g^{-1} or 0.27 F cm^{-2}), nanospheres (200 F g^{-1} or 0.2 F cm^{-2}) as well as CC (5.9 F g^{-1} or 0.07 F cm^{-2}, Fig. S6), demonstrating the good sodium storage performance of the nanotubes. According to above results, the pore volume and specific surface area of Nb_2O_5 nanotubes are the highest among all the electrode materials, which contributes to increasing the contacting area of electrode materials and electrolyte and improves

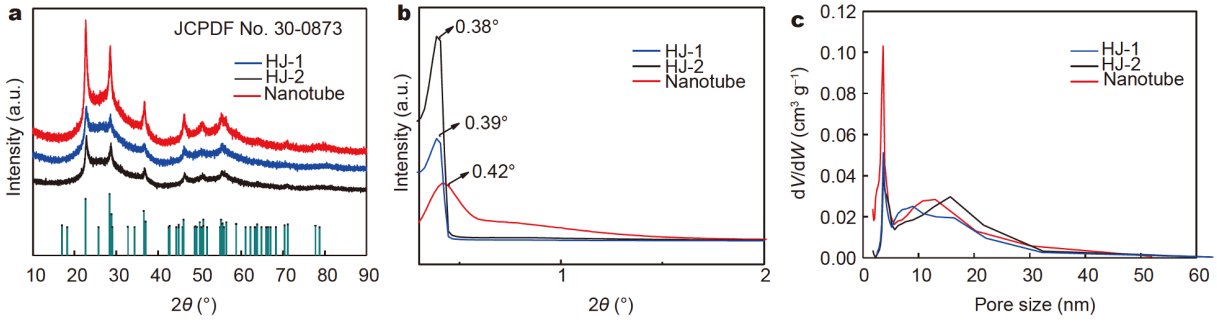

Figure 4 (a) XRD patterns, (b) SAXS and (c) pore size distributions of the Nb-based products with various nanostructures.

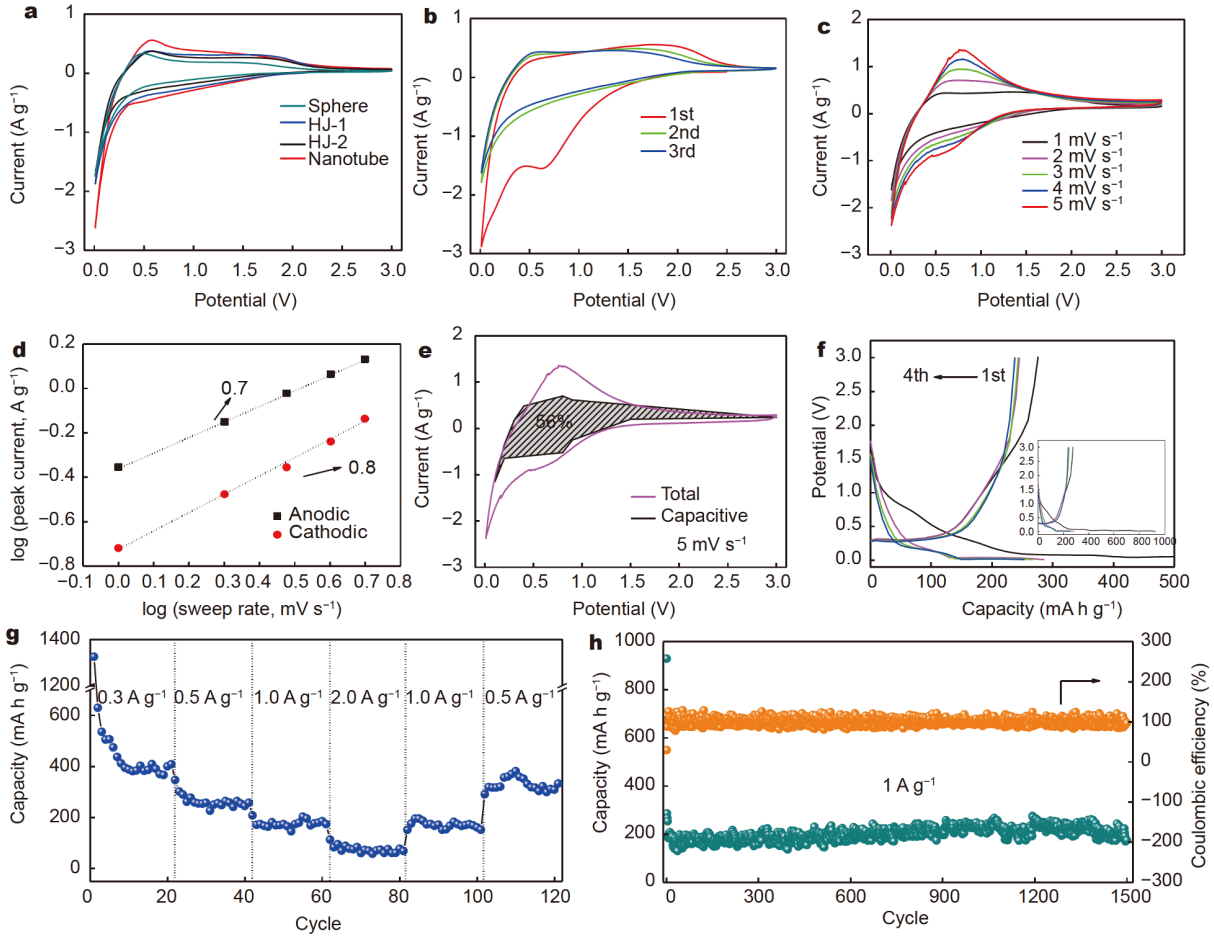

Figure 5 Electrochemical performances of the Nb-based products in Na-ion half cells: (a) CV curves of the Nb_2O_5@CC products with different nanostructures at the scan rate of 1 mV s^{-1}. (b) CV curves of the Nb_2O_5@CC nanotubes for the first three cycles at the scan rate of 1 mV s^{-1}. (c, d) CV curves and specific peak current of the Nb_2O_5@CC nanotubes at different scan rates from 1 to 5 mV s^{-1}. (e) CV curve of the Nb_2O_5@CC nanotubes with the shaded area of surface capacitive contribution at 5 mV s^{-1}. (f) GCD profiles of the Nb_2O_5@CC nanotubes at 1 A g^{-1}. (g) Rate capability of the Nb_2O_5@CC nanotubes at various current densities. (h) Long-term cycling stability of the Nb_2O_5@CC nanotubes at 1 A g^{-1}.

the sodium-storage performance. Thus we chose Nb_2O_5@CC nanotubes as the optimal electrode materials for the following in-depth investigations in SICs.

Fig. 5b displays the first three CV curves of the Nb_2O_5@CC nanotubes at the sweep rate of 1 mV s^{-1}. In the first intercalation process, the obvious cathodic peak at the potential of 1.5–0.5 V manifests the solid-electrolyte interphase (SEI) film with other side reactions occurring. Meanwhile, it also consists the peak of pure CC at around 0.85 V (Fig. S6) [32]. During the de-intercalation process of Na^+, the broad peaks from 1.5 to 2.0 V confirm the oxidation reaction of Nb^{4+} to Nb^{5+} [33]. According to the XPS analyses of the Nb_2O_5@CC at fully discharged and charged states (Fig. S7), the Nb $3d_{3/2}$ and Nb $3d_{5/2}$ peaks at 210.2 and 207.5 eV, respectively, shifted to lower positions of 209.5 and 206.8 eV (Nb^{4+}) when it was fully discharged. Oppositely, when it was at fully charged state, the peaks basically recovered to the pristine value, which demonstrated the reversible electrochemical reactions of Nb [34]. After the first charging/discharging process, the second and the third cycles were almost restorable, implying that the electrochemical reactions were reversible. Based on the above results, the Na^+ intercalation/de-intercalation reaction in Nb_2O_5@CC nanotubes could be supposed to:

$$Nb_2O_5 + xNa^+ + xe^- \leftrightarrow Na_xNb_2O_5 \quad (2)$$

where x represents the stoichiometric number of sodium ions, similar to those in LICs, LIBs, sodium ion and potassium ion batteries [33–40].

In order to investigate the Na^+ storage kinetics, the CV curves were carried out in the voltage of 0.01–3.0 V at various scan rates of 1–5 mV s^{-1}, as exhibited in Fig. 5c.

The similar shape of the CV curves indicates that the electrochemical reactions are involved in the Na^+ insertion/extraction. Since Nb_2O_5 is a typical pseudocapacitance material, the electrochemical capacity usually includes two parts. One is the diffusion-controlled value and the other is surface capacitive contribution. And the formula is generally described as:

$$i = av^b, \quad (3)$$

in which a, b represent the appropriate parameters, i is the current (A g^{-1}) and v is the scan rate (mV s^{-1}). The b-value can classify the process of diffusion-controlled insertion and surface capacitance in the electrochemical reactions. When the b-value is near 0.5, the diffusion-controlled behavior has a great influence, while the b-value of 1 suggests a total capacitance-controlled reaction [41]. As displayed in Fig. 5d, the b-values of anodic and cathodic peaks were calculated to be 0.7 and 0.8, respectively, demonstrating the diffusion-controlled insertion and surface capacity coexisted. More importantly, Dunn *et al.* [42] put forward that the specific contributions from diffusion-controlled insertion and surface capacitive reactions can be quantitatively calculated with the formula as follow:

$$i = k_1v+k_2v^{1/2}, \quad (4)$$

where k_1 and k_2 represent the adjustable values. It is worth noting that the proportion of surface capacitive as well as diffusion-controlled insertion contributions can be obtained through k_1v and $k_2v^{1/2}$ values at a prescribed potential. In this way, Fig. 5e shows that 56% of the total capacity origins from the surface capacitive reactions. According to ex-XPS results of Nb element in electrode materials after fully discharged/charged cycles, the reaction of Nb^{5+} to Nb^{4+} appeared when the device was fully discharged, illustrating that the behavior of Na^+ insertion appeared during the discharging process [16,42–44]. Moreover, as the voltage decreased, the number of intercalated sodium ions gradually increased. From the CV curves, the diffusion-controlled insertion predominantly occurred below 0.2 V, demonstrating that the diffusion process was facile at low potentials. In addition, Nb_2O_5 is a pseudocapacitve material. The high specific surface area is beneficial to improving the surface capacitive contribution in the shaded area. Meanwhile, the initial four GCD curves at 1 A g^{-1} were also performed in Fig. 5f. The Nb_2O_5@CC nanotubes delivered an original discharging and charging capacities of 929 and 275 mA h g^{-1} with the coulombic efficiency of 30%. Fig. 5g exhibits the rate performance of Nb_2O_5@CC nanotubes varying from 0.3 to 2 A g^{-1}. When it was cycled at high current densities of 1 and 2 A g^{-1}, the specific capacities of 177 and 86 mA h g^{-1} can still be obtained, exhibiting decent rate properties of the Nb_2O_5@CC nanotubes. The long-term cycling properties and the coulombic efficiency of Nb_2O_5@CC nanotubes were tested, as shown in Fig. 5h. After 1500 cycles, the capacity of 175 mA h g^{-1} still remained with coulombic efficiency of 97%, higher than that of m-Nb_2O_5/C electrode materials (125 mA h g^{-1} at 1 A g^{-1} cycling for 1000 times) [45], demonstrating good sodium-storage performance of the nanotubes. In addition, by contrast with commercial Nb_2O_5, the as-synthesized Nb_2O_5@CC nanotubes also displayed enhanced sodium-storage performance such as specific capacitance and cycling stability (Fig. S8).

In order to investigate the potential applications of the Nb_2O_5@CC nanotubes as electrode in SICs, a common AC material was chosen as the other electrode to assemble a hybrid SIC. Fig. S9 further compares the CV curves of Nb_2O_5 nanotubes and AC electrodes on the CC at 10 mV s^{-1} in sodium-ion half cells. Obviously, Nb_2O_5 and AC electrodes possess stable voltage windows between 0.01–3.0 V and 3–4.3 V, respectively. To obtain charge balance, the optimized mass ratio of the electrodes (m_{anode} and $m_{cathode}$) can be described with the equation [46]:

$$\frac{m_{cathode}}{m_{anode}} = \frac{C_{anode}}{C_{cathode}} \times \frac{\Delta E_{anode}}{\Delta E_{cathode}}, \quad (5)$$

where m, C and ΔE represent the weight, capacitance and the voltage range of the electrodes in the discharge process. Thus, the optimized mass ratio between the anode and cathode was 1:2 and the relevant voltage testing window of the SICs was set at 0–4.0 V to avoid the decomposition of electrolyte. Before assembling the SIC devices, the tubular Nb_2O_5@CC electrode was pre-cycled for three times with Na chip at 0.1 A g^{-1} in half cells and then discharged to 0.1 V to finish the pre-sodiation. After disassembling, the pre-sodiated tubular Nb_2O_5@CC material was used as anode in the SICs. Through this process, the pre-sodiated tubular Nb_2O_5@CC film can not only achieve stable state but also reduce the consumption of excessive electrolyte in SICs. The CV curves in Fig. S10 displays distorted rectangular shapes, which could be explained with the mechanism of the SICs that combined the features of SCs and batteries [47]. Fig. 6a shows the GCD curves of Nb_2O_5//AC based SIC from 0 to 4.0 V at the specific current densities of 0.03–0.3 A g^{-1}. The symmetrical triangular shape with a low iR drop illustrated a high coulombic efficiency of the device. The calculation formula of capacitance based on GCD curve is:

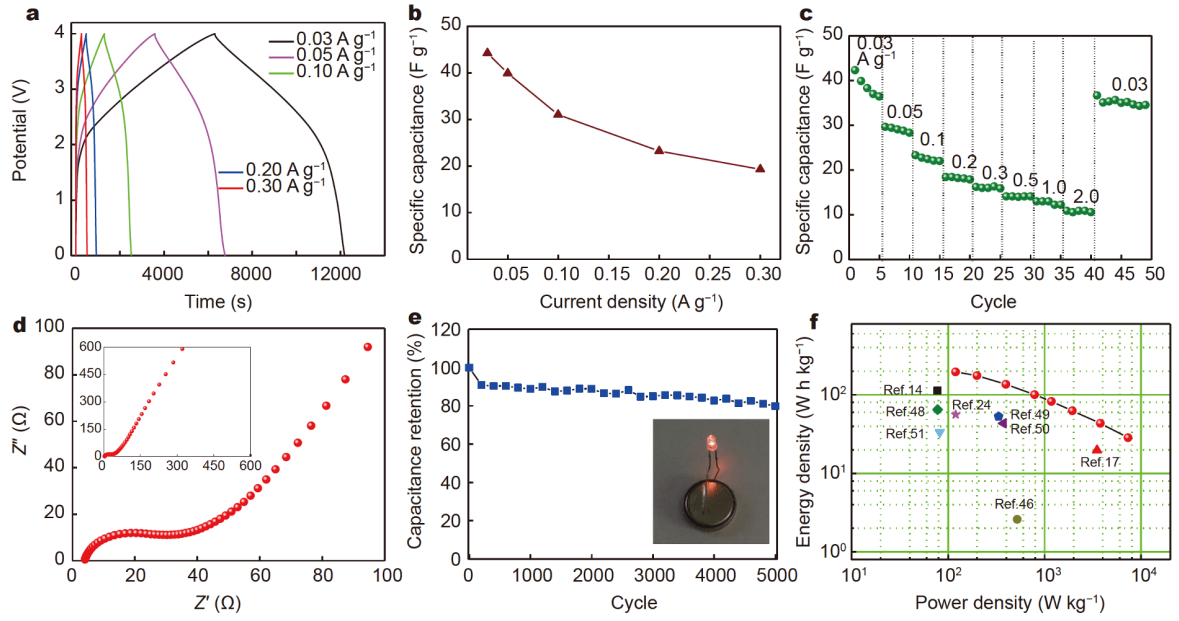

Figure 6 Electrochemical performance of the SICs using Nb_2O_5@CC nanotubes as anode and AC as cathode: (a) GCD curves of the SICs at different current densities from 0.03 to 0.3 A g^{-1}. (b) Specific capacitance as a function of various current densities. (c) The rate performance tested by progressively changing the current densities. (d) The high-frequency region of the Nyquist impedance plot. The inset shows the Nyquist impedance plot of the SICs. (e) The long cycling stability of the SICs. The inset displays a photograph of an LED lighted by a coin SIC device. (f) Energy and power densities of the fabricated SICs.

$$C = i \times t / (m \times \Delta E), \quad (6)$$

in which C is the capacitance, i is the current, t is the discharging time, m is the total mass of active materials and ΔE is the voltage change during the discharging process. The calculated specific capacitances of the device are displayed in Fig. 6b, where the largest specific capacitance of the prepared SICs is 44.2 F g^{-1} at 0.03 A g^{-1}, superior to V_2O_5/CNT//AC Na-ion supercapacitors (35 F g^{-1}) [12]. Furthermore, Fig. 6c displays the rate performance of the SICs through progressively changing the current densities. The average specific capacitances of the device are 38.8, 29.1, 22.5, 18.2, 16.1, 14.1, 12.7, 10.8 and 35.2 F g^{-1} at 0.03, 0.05, 0.1, 0.2, 0.3, 0.5, 1, 2 and 0.03 A g^{-1}, respectively. That is to say, 90.7% of the capacitance still remained when it came back to the original current density, implying the good rate properties of the fabricated SIC devices. Fig. 6d presents the electrochemical impedance spectroscopy (EIS) of the SICs with frequencies from 100 kHz to 0.01 Hz. The internal resistance was about 4 Ω, illustrating that the electrode materials had good contact with the electrolyte. Besides, the cycling stability of the SIC was conducted in this work. As displayed in Fig. 6e, the designed SIC exhibited good cycling performance with 80% capacitance retention of the original value at 5 A g^{-1} after 5000 cycles. According to the calculation formulas of power (W kg^{-1}) and energy (W h kg^{-1}) densities of SICs:

$$P = \Delta V \times i / m, \quad (7)$$

$$E = P \times t / 3600, \quad (8)$$

$$\Delta V = (V_{max} + V_{min}) / 2, \quad (9)$$

where i, t, V_{max} and V_{min} represents the current, time, the maximum voltage after the iR drop and the final potential in the discharging process. In Fig. 6f, the energy density was calculated as high as 195 W h kg^{-1} at 120 W kg^{-1} and the maximum power density of 7328 W kg^{-1} at 28 W h kg^{-1}, superior to the previous reports of λ-MnO_2//AC (19.7 W h kg^{-1} at 3500 W kg^{-1}), V_2O_5 nanorods@rGO//AC (65 W h kg^{-1} at 72 W kg^{-1}), $NaTi_2(PO_4)_3$/rGO//AC (53 W h kg^{-1} at 334 W kg^{-1}), core-shell Gr-Nb_2O_5//AC (112.9 W h kg^{-1} at 80.1 W kg^{-1}), sandwich-like G@mNb_2O_5//AC (56.1 W h kg^{-1} at 120 W kg^{-1}) in SICs and T-Nb_2O_5 nanowires@CC//GA (2.6 W h kg^{-1} at 521.7 W kg^{-1}), C-T-Nb_2O_5 nanowires//AC (43.4 W h kg^{-1} at 374.98 W kg^{-1}), CNT-Nb_2O_5//AC (33.5 W h kg^{-1} at 82 W kg^{-1}) in LICs [14,17,24,46,48–51]. Significantly, the hierarchical structure of Nb_2O_5@CC nanotubes shown in Figs 1 and 2a, b with the features of increased electrical conductivity, alleviated volume expansion during the insertion/extraction process and shortened ion transport pathway, can efficiently improve the Na-ion storage

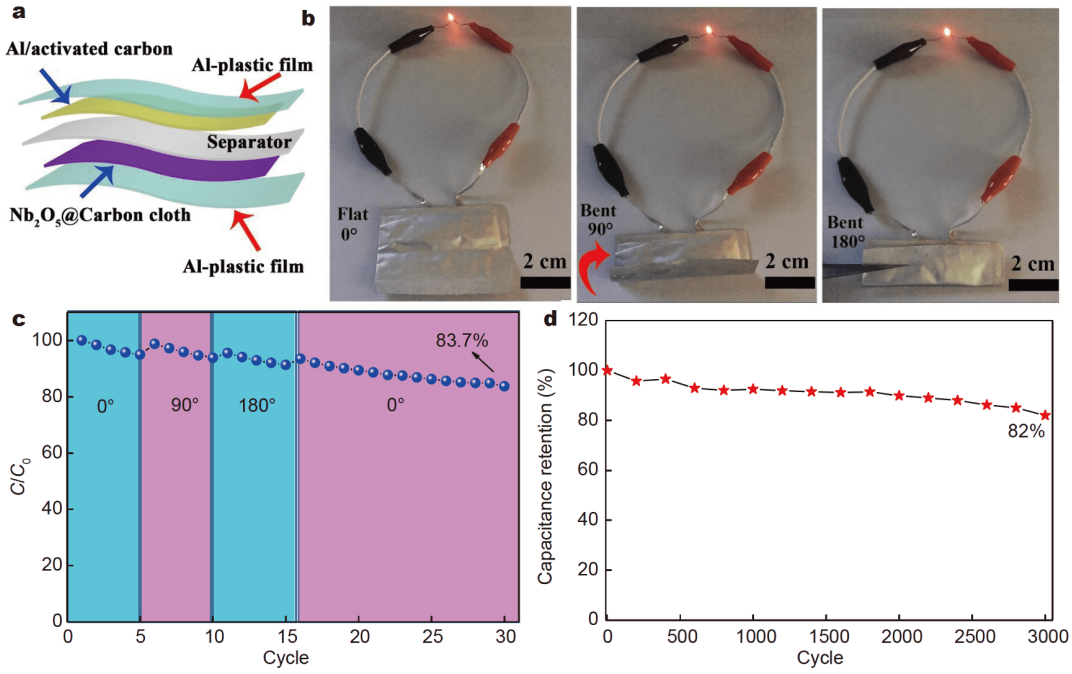

Figure 7 The properties of flexible SIC devices based on the tubular Nb_2O_5@CC//AC electrodes. (a) Schematic diagram of the device. (b) Photographs of the flexible device powering LED under different bending angles. (c) Cycling properties of the bendable SICs at different bending conditions. (d) Long-term cycling performance of the device without bending.

performances of the fabricated SICs including high specific capacitance, long lifespan and good rate capability.

The tubular Nb_2O_5@CC//AC based SIC was further encapsulated in flexible package for its promising application in the wearable energy storage field. Fig. 7a shows the schematic diagram of the device. The Nb_2O_5@CC nanotubes and AC electrodes sandwiched by a separator were packed in the Al-plastic film. To investigate the practicality of the flexible SIC, a light emitting diode (LED) lamp was connected with this device. Fig. 7b displays the photographs of the circuit. Clearly, the LED lamp was lighted normally by the flexible SICs under various bending states of 0°, 90°, and 180°, respectively. After continually bending-flat measurement for 30 cycles, 83.7% of the initial capacitance still retained, as shown in Fig. 7c. All of the results above illustrate the good mechanical flexibility and electrochemical stability of our flexible SIC devices. Furthermore, Fig. 7d exhibits that after 3000 cycles, the capacitance remains 82% of the original value, demonstrating good cycling performance and potential applications of the SICs in flexible and wearable electric devices.

CONCLUSION

In summary, by adjusting the pH value, Nb_2O_5 nanotubes and homo-junctions successfully germinated on CC through a straightforward hydrothermal process in the presence of pyridine. The as-prepared Nb_2O_5@CC nanotubes displayed superior electrochemical properties including high rate capacity and good cycling stability among several electrodes with various morphologies. Such Nb_2O_5@CC nanotubes with a large surface area have three advantages: (i) utilizing CC to improve the conductivity of the device; (ii) alleviating the volume expansion during the insertion/extraction process; (iii) infiltrating electrolyte to attain good contact. In addition, the fabricated tubular Nb_2O_5@CC//AC SICs were measured with a high energy density of 195 W h kg^{-1} at 120 W kg^{-1} and the maximum power density of 7328 W kg^{-1} at 28 W h kg^{-1}. Furthermore, the prototype of flexible SICs was designed with stable electrochemical performance at different bending states. All these results indicate that the fabricated Nb_2O_5@CC//AC SICs can be a promising candidate in future energy storage applications.

Received 17 January 2020; accepted 24 February 2020; published online 7 April 2020

1 Liu Y, Wang H, Cheng L, *et al.* TiS_2 nanoplates: A high-rate and stable electrode material for sodium ion batteries. Nano Energy,

2016, 20: 168–175
2 Wang L, Wang K, Lou Z, *et al.* Plant-based modular building blocks for "green" electronic skins. Adv Funct Mater, 2018, 28: 1804510
3 Wang L, Chen D, Jiang K, *et al.* New insights and perspectives into biological materials for flexible electronics. Chem Soc Rev, 2017, 46: 6764–6815
4 Bruce PG, Freunberger SA, Hardwick LJ, *et al.* Li–O_2 and Li–S batteries with high energy storage. Nat Mater, 2011, 11: 19–29
5 Thangavel R, Moorthy B, Kim DK, *et al.* Pushing the energy output and cyclability of sodium hybrid capacitors at high power to new limits. Adv Energy Mater, 2017, 7: 1602654
6 Yang S, Han Z, Zheng F, *et al.* $ZnFe_2O_4$ nanoparticles-cotton derived hierarchical porous active carbon fibers for high rate-capability supercapacitor electrodes. Carbon, 2018, 134: 15–21
7 Zuo W, Li R, Zhou C, *et al.* Battery-supercapacitor hybrid devices: recent progress and future prospects. Adv Sci, 2017, 4: 1600539
8 Wang H, Zhu C, Chao D, *et al.* Nonaqueous hybrid lithium-ion and sodium-ion capacitors. Adv Mater, 2017, 29: 1702093
9 Choi C, Ashby DS, Butts DM, *et al.* Achieving high energy density and high power density with pseudocapacitive materials. Nat Rev Mater, 2020, 5: 5–19
10 Zhang L, Wei Q, Sun D, *et al.* Conversion reaction of vanadium sulfide electrode in the lithium-ion cell: Reversible or not reversible? Nano Energy, 2018, 51: 391–399
11 Wei Q, Jiang Y, Qian X, *et al.* Sodium ion capacitor using pseudocapacitive layered ferric vanadate nanosheets cathode. iScience, 2018, 6: 212–221
12 Chen Z, Augustyn V, Jia X, *et al.* High-performance sodium-ion pseudocapacitors based on hierarchically porous nanowire composites. ACS Nano, 2012, 6: 4319–4327
13 Babu B, Ullattil SG, Prasannachandran R, *et al.* Ti^{3+} induced brown TiO_2 nanotubes for high performance sodium-ion hybrid capacitors. ACS Sustain Chem Eng, 2018, 6: 5401–5412
14 Wang X, Li Q, Zhang L, *et al.* Caging Nb_2O_5 nanowires in PECVD-derived graphene capsules toward bendable sodium-ion hybrid supercapacitors. Adv Mater, 2018, 30: 1800963
15 Zhu YE, Yang L, Sheng J, *et al.* Fast sodium storage in TiO_2@CNT@C nanorods for high-performance Na-ion capacitors. Adv Energy Mater, 2017, 7: 1701222
16 Lim E, Jo C, Kim MS, *et al.* High-performance sodium-ion hybrid supercapacitor based on Nb_2O_5@carbon core-shell nanoparticles and reduced graphene oxide nanocomposites. Adv Funct Mater, 2016, 26: 3711–3719
17 Zhang Y, Yuan C, Ye K, *et al.* An aqueous capacitor battery hybrid device based on Na-ion insertion-deinsertion in λ-MnO_2 positive electrode. Electrochim Acta, 2014, 148: 237–243
18 Dong J, Jiang Y, Li Q, *et al.* Pseudocapacitive titanium oxynitride mesoporous nanowires with iso-oriented nanocrystals for ultra-high-rate sodium ion hybrid capacitors. J Mater Chem A, 2017, 5: 10827–10835
19 Wang R, Wang S, Peng X, *et al.* Elucidating the intercalation pseudocapacitance mechanism of MoS_2–carbon monolayer interoverlapped superstructure: toward high-performance sodium-ion-based hybrid supercapacitor. ACS Appl Mater Interfaces, 2017, 9: 32745–32755
20 Chauhan H, Singh MK, Kumar P, *et al.* Development of SnS_2/RGO nanosheet composite for cost-effective aqueous hybrid supercapacitors. Nanotechnology, 2016, 28: 025401
21 Liu X, Wang H, Cui Y, *et al.* High-energy sodium-ion capacitor assembled by hierarchical porous carbon electrodes derived from Enteromorpha. J Mater Sci, 2018, 53: 6763–6773
22 Xie X, Zhao MQ, Anasori B, *et al.* Porous heterostructured MXene/carbon nanotube composite paper with high volumetric capacity for sodium-based energy storage devices. Nano Energy, 2016, 26: 513–523
23 Wei T, Yang G, Wang C. Iso-oriented $NaTi_2(PO_4)_3$ mesocrystals as anode material for high-energy and long-durability sodium-ion capacitor. ACS Appl Mater Interfaces, 2017, 9: 31861–31870
24 Tong Z, Liu S, Zhou Y, *et al.* Rapid redox kinetics in uniform sandwich-structured mesoporous Nb_2O_5/graphene/mesoporous Nb_2O_5 nanosheets for high-performance sodium-ion supercapacitors. Energy Storage Mater, 2018, 13: 223–232
25 Su D, Wang G. Single-crystalline bilayered V_2O_5 nanobelts for high-capacity sodium-ion batteries. ACS Nano, 2013, 7: 11218–11226
26 Ali RF, Nazemi AH, Gates BD. Surfactant controlled growth of niobium oxide nanorods. Cryst Growth Des, 2017, 17: 4637–4646
27 Liu F, Xue D. Fabrication of Nb_2O_5 nanotrees with controlled branching degrees. Phys Scr, 2010, T139: 014074
28 Lim E, Jo C, Kim H, *et al.* Facile synthesis of Nb_2O_5@carbon core–shell nanocrystals with controlled crystalline structure for high-power anodes in hybrid supercapacitors. ACS Nano, 2015, 9: 7497–7505
29 Wu J, Xue D. Localized crystallization: a chemical transformation of Nb_2O_5 rod-like arrays into ordered niobate arrays. CrystEngComm, 2011, 13: 1966–1975
30 Liu J, Xue D, Li K. Single-crystalline nanoporous Nb_2O_5 nanotubes. Nanoscale Res Lett, 2011, 6: 138
31 Suzuki N, Athar T, Huang YT, *et al.* Synthesis of mesoporous Nb_2O_5 with crystalline walls and investigation of their photocatalytic activity. J Ceram Soc Jpn, 2011, 119: 405–411
32 Hou X, Liu B, Wang X, *et al.* SnO_2-microtube-assembled cloth for fully flexible self-powered photodetector nanosystems. Nanoscale, 2013, 5: 7831–7837
33 Lin J, Yuan Y, Su Q, *et al.* Facile synthesis of Nb_2O_5/carbon nanocomposites as advanced anode materials for lithium-ion batteries. Electrochim Acta, 2018, 292: 63–71
34 Li N, Zhang F, Tang Y. Hierarchical T-Nb_2O_5 nanostructure with hybrid mechanisms of intercalation and pseudocapacitance for potassium storage and high-performance potassium dual-ion batteries. J Mater Chem A, 2018, 6: 17889–17895
35 Zhao Y, Ding C, Hao Y, *et al.* Neat design for the structure of electrode to optimize the lithium-ion battery performance. ACS Appl Mater Interfaces, 2018, 10: 27106–27115
36 Mokhlesur Rahman M, Zhou M, Sultana I, *et al.* Additive-free Nb_2O_5–TiO_2 hybrid anode towards low-cost and safe lithium-ion batteries: A green electrode material produced in an environmentally friendly process. Batteries Supercaps, 2019, 2: 160–167
37 Kong F, Tao S, Qian B, *et al.* Multiwalled carbon nanotube-modified Nb_2O_5 with enhanced electrochemical performance for lithium-ion batteries. Ceramics Int, 2018, 44: 23226–23231
38 Cheong JY, Youn DY, Kim C, *et al.* Ag-coated one-dimensional orthorhombic Nb_2O_5 fibers as high performance electrodes for lithium storage. Electrochim Acta, 2018, 269: 388–396
39 Yu H, Xu L, Wang H, *et al.* Nanochannel-confined synthesis of Nb_2O_5/CNTs nanopeapods for ultrastable lithium storage. Electrochim Acta, 2019, 295: 829–834
40 Yoo Y, Kang YC. Mesoporous Nb_2O_5 microspheres with filled and

yolk-shell structure as anode materials for lithium-ion batteries. J Alloys Compd, 2019, 776: 722–730
41 Yang H, Xu R, Gong Y, *et al.* An interpenetrating 3D porous reticular Nb_2O_5@carbon thin film for superior sodium storage. Nano Energy, 2018, 48: 448–455
42 Wang J, Polleux J, Lim J, *et al.* Pseudocapacitive contributions to electrochemical energy storage in TiO_2 (anatase) nanoparticles. J Phys Chem C, 2007, 111: 14925–14931
43 He P, Quan Y, Xu X, *et al.* High-performance aqueous zinc-ion battery based on layered $H_2V_3O_8$ nanowire cathode. Small, 2017, 13: 1702551
44 Meng J, He Q, Xu L, *et al.* Identification of phase control of carbon-confined Nb_2O_5 nanoparticles toward high-performance lithium storage. Adv Energy Mater, 2019, 9: 1802695
45 Wu Y, Fan X, Gaddam RR, *et al.* Mesoporous niobium pentoxide/carbon composite electrodes for sodium-ion capacitors. J Power Sources, 2018, 408: 82–90
46 Zhang J, Chen H, Sun X, *et al.* High intercalation pseudocapacitance of free-standing T-Nb_2O_5 nanowires@carbon cloth hybrid supercapacitor electrodes. J Electrochem Soc, 2017, 164: A820–A825
47 Dong G, Wang H, Liu W, *et al.* Nitrate salt assisted fabrication of highly N-doped carbons for high-performance sodium ion capacitors. ACS Appl Energy Mater, 2018, 1: 5636–5645
48 R. K, C. N, R. K, *et al.* Reduced graphene oxide embedded V_2O_5 nanorods and porous honey carbon as high performance electrodes for hybrid sodium-ion supercapacitors. Electrochim Acta, 2017, 256: 221–231
49 Roh HK, Kim MS, Chung KY, *et al.* A chemically bonded $NaTi_2(PO_4)_3$/rGO microsphere composite as a high-rate insertion anode for sodium-ion capacitors. J Mater Chem A, 2017, 5: 17506–17516
50 Wang X, Yan C, Yan J, *et al.* Orthorhombic niobium oxide nanowires for next generation hybrid supercapacitor device. Nano Energy, 2015, 11: 765–772
51 Wang X, Li G, Chen Z, *et al.* High-performance supercapacitors based on nanocomposites of Nb_2O_5 nanocrystals and carbon nanotubes. Adv Energy Mater, 2011, 1: 1089–1093

Acknowledgements This work was supported by the National Natural Science Foundation of China (51672308, 51972025 and 61888102).

Author contributions The paper was written through contributions of all authors. All authors have given approval to the final version of the paper.

Conflict of interest The authors declare no conflict of interest.

Supplementary information Supporting data are available in the online version of the paper.

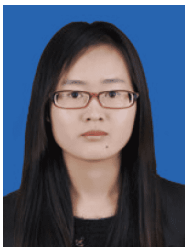

Rui Jia received her BE degree in 2015 from Huaqiao University and ME degree in 2018 from Qingdao University. She is a PhD candidate at the College of Mathematics and Physics, University of Science and Technology Beijing, China. Her research interests mainly focus on sodium-ion batteries and hybrid supercapacitors.

Guozhen Shen received his BSc degree (1999) in chemistry from Anhui Normal University and PhD degree (2003) in chemistry from the University of Science and technology of China. He joined the Institute of Semiconductors, Chinese Academy of Sciences as a Professor in 2013. His current research focuses on the flexible electronics and printable electronics, including transistors, photodetectors, sensors and flexible energy storage and conversion devices.

Di Chen received her BSc degree (1999) in chemistry from Anhui Normal University and PhD degree (2005) in chemistry from the University of Science and technology of China. She joined the University of Science and Technology Beijing as a Professor in 2014. Her current research focuses on the energy storage materials and devices.

基于碳布上直接生长的Nb_2O_5纳米管的高性能钠离子电容器

贾蕊[1,2], 姜源[3], 李蕊[1], 柴瑞青[2], 娄正[2], 沈国震[2*], 陈娣[1*]

摘要 钠离子混合电容器是连接超级电容器与电池之间的桥梁, 在大规模储能领域中具有广阔的应用前景. 然而, 设计出能够与正极材料相匹配, 并且兼具快速动力学行为和长循环寿命的负极材料仍然是目前面临的重要挑战之一. 本文通过简单的水热工艺, 通过调节溶液的pH值, 可以将Nb_2O_5纳米管以及纳米线/纳米管同质结直接生长在碳布 (CC) 上. 所制备的Nb_2O_5@CC纳米管在1500次循环后, 电流密度为1 A g^{-1}时表现出175 mA h g^{-1}的高可逆容量以及97%的库伦效率. 以Nb_2O_5@CC为负极、活性炭为正极制备的钠离子混合电容器的能量密度和功率密度分别可达到195 W h kg^{-1}和7328 W kg^{-1}. 即使在5000次循环后仍然具有80%的电容保持率. 另外, 该柔性钠离子混合电容器可以在各种可弯曲条件下正常工作. 因此, Nb_2O_5@CC纳米管在未来有望成为一种柔性可穿戴能源存储器的理想电极材料.

